

See discussions, stats, and author profiles for this publication at: <https://www.researchgate.net/publication/51680277>

Fine Tuning the Energetics of Excited-State Intramolecular Proton Transfer (ESIPT): White Light Generation in A Single ESIPT System

ARTICLE *in* JOURNAL OF THE AMERICAN CHEMICAL SOCIETY · SEPTEMBER 2011

Impact Factor: 12.11 · DOI: 10.1021/ja2062693 · Source: PubMed

CITATIONS

101

READS

60

9 AUTHORS, INCLUDING:



Kew-Yu Chen

Feng Chia University

66 PUBLICATIONS 822 CITATIONS

SEE PROFILE



Wen-Yi Hung

National Taiwan Ocean University

64 PUBLICATIONS 1,587 CITATIONS

SEE PROFILE

Fine Tuning the Energetics of Excited-State Intramolecular Proton Transfer (ESIPT): White Light Generation in A Single ESIPT System

Kuo-Chun Tang,[†] Ming-Jen Chang,[‡] Tsung-Yi Lin,[†] Hsiao-An Pan,[†] Tzu-Chien Fang,[‡] Kew-Yu Chen,^{*,‡} Wen-Yi Hung,^{*,§} Yu-Hsiang Hsu,[§] and Pi-Tai Chou^{*,†}

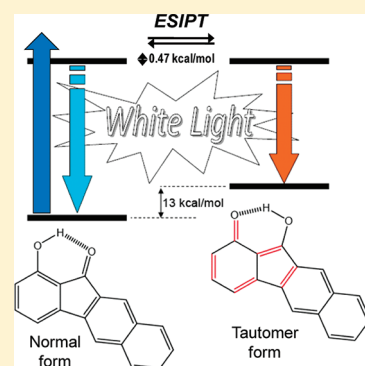
[†]Department of Chemistry, National Taiwan University, Taipei, 10617 Taiwan, R.O.C.

[‡]Department of Chemical Engineering, Feng Chia University, Taichung, 40724 Taiwan, R.O.C.

[§]Institute of Optoelectronic Sciences, National Taiwan Ocean University, Keelung, 20224 Taiwan, R.O.C.

 Supporting Information

ABSTRACT: Using 7-hydroxy-1-indanone as a prototype (**I**), which exhibits excited-state intramolecular proton transfer (ESIPT), chemical modification has been performed at C(2)–C(3) positions by fusing benzene (molecule **II**) and naphthalene rings, (molecule **III**). **I** undergoes an ultrafast rate of ESIPT, resulting in a unique tautomer emission ($\lambda_{\text{max}} \sim 530$ nm), whereas excited-state equilibrium is established for both **II** and **III**, as supported by the dual emission and the associated relaxation dynamics. The forward ESIPT (normal to proton-transfer tautomer species) rates for **II** and **III** are deduced to be $(30 \text{ ps})^{-1}$ and $(22 \text{ ps})^{-1}$, respectively, while the backward ESIPT rates are $(11 \text{ ps})^{-1}$ and $(48 \text{ ps})^{-1}$. The ESIPT equilibrium constants are thus calculated to be 0.37 and 2.2 for **II** and **III**, respectively, giving a corresponding free energy change of 0.59 and -0.47 kcal/mol between normal and tautomer species. For **III**, normal and tautomer emissions in solid are maximized at 435 and 580 nm, respectively, achieving a white light generation with Commission Internationale de l'Eclairage (CIE) (0.30, 0.27). An organic light-emitting diode based on **III** is also successfully fabricated with maximum brightness of 665 cd m^{-2} at 20 V (885 mA cm^{-2}) and the CIE coordinates of (0.26, 0.35). The results provide the proof of concept that the white light generation can be achieved in a single ESIPT system.



1. INTRODUCTION

Excited-state intramolecular proton transfer (ESIPT) has long been an issue of fundamental importance.¹ Most of the ESIPT reactions involve proton (on hydrogen atom) transfer from a pre-existing hydrogen bond, giving rise to a proton-transfer tautomer in the excited state. Due to the drastic structural alternation, the tautomer possesses different photophysical properties from that of the original (normal) species, offering great versatility in a variety of applications, such as lasing materials,² UV photostabilizer,³ optical filter,⁴ radiation scintillator,⁵ molecular recognition,⁶ etc. Most recent cutting edge application seems to be focusing on the lighting materials.⁷ The ultrafast rate of ESIPT, together with a large Stokes shift between absorption and tautomer emission (peak-to-peak), provides a broad spectral window to fill in other complementary emission color free from energy transfer and reabsorption. Also, due to the near UV absorption, the naked eye's view of the film is transparent, beneficial to its versatility in commercial applications.

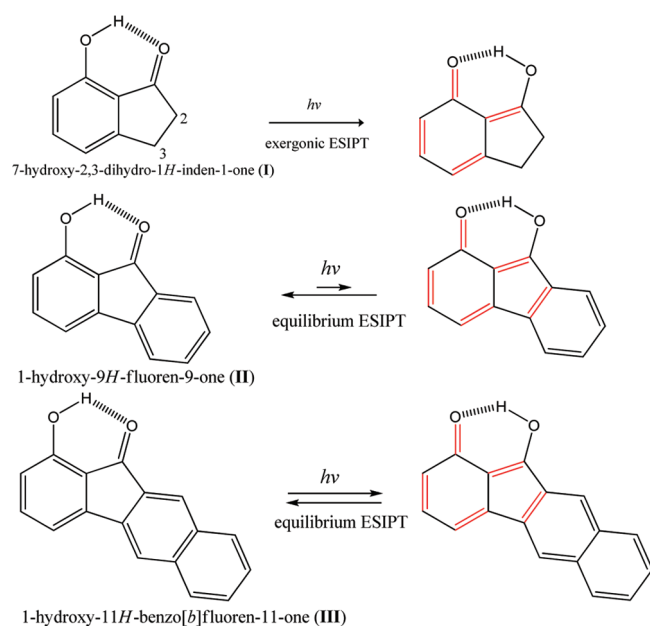
Along the above advantages, attempts exploiting ESIPT molecules to attain white light generation have recently been made.⁷ Via mixing two ESIPT molecules, dual proton-transfer emission and hence color hue can be ratiometrically fine-tuned.^{7a} Park and co-workers reported the white-emitting molecules comprised of covalently linked blue and yellow color-emitting ESIPT moieties.^{7b,c} Sun et al. reported a white light generation

combining solid polymers doped with ESIPT molecules.^{7d} Very recently, via anchoring the designated ESIPT molecules onto ultrasmall CdSe quantum dots, we reported white light generation of the resulting nanocomposites with the fascinating Commission Internationale de l'Eclairage (CIE) coordinate of (0.33, 0.33).^{7e} Unfortunately, mixing multiple emissive materials commonly requires a delicate balance between chromophores in terms of emission and excitation to attain a white light. Also, spectral variation may arise due to different photostability and environmental perturbation onto different chromophores upon long-term use. Needless to say, the more emissive materials are used, the more cost ineffective the device is.

Thus, further advancement may lie in searching for a single ESIPT system that is able to render both normal and tautomer emissions intrinsically, spanning the entire visible region suited for white light generation. Unfortunately, most ESIPT molecules possess a strong intramolecular hydrogen bond, so that ESIPT is either barrierless or small; its time scale is generally $<1 \text{ ps}$,¹ resulting in a lack of normal emission. If there is any exception, one class of ESIPT system exhibiting dual emission should be credited to recently developed excited-state proton coupled charge-transfer molecules,^{1b} for which either normal or tautomer

Received: July 6, 2011

Published: September 29, 2011

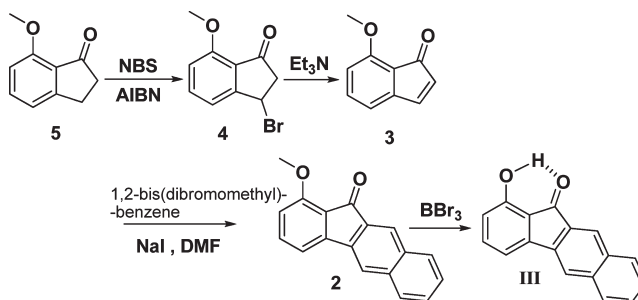
Scheme 1. Structures and ESIPT Mechanism of Systems I, II, and III^a

^a Note that the effective conjugated double bonds responsible for the proton-transfer tautomer emission are marked in red.

species possesses strong charge-transfer character, giving a drastic difference in dipole moment between normal and tautomer forms. Accordingly, in solution, solvent reorganization may channel into the reaction, inducing a barrier that leads to slow ESIPT and hence dual emission. Unfortunately, the prohibition of molecular skeleton relaxation in rigid media hampers further fabrication toward solid devices.

In this study, we then switched the research direction toward harnessing the thermodynamics of ESIPT. Our tactic is to systematically fine-tune the energetics of a series of designed ESIPT molecules, so that thermal equilibrium can be reached between normal and tautomer species in the excited state. If the pre-equilibrium can be established prior to their respective population deactivation, we then expect a dual (normal and tautomer) emission covering the designated visible range.

Herein, we report the strategic design and synthesis of a series of potential ESIPT molecules **I**, **II**, and **III**, in which **II** and **III** are chemical modifications of the ESIPT system **I** (7-hydroxy-1-indanone)⁸ at C(2)–C(3) positions (see Scheme 1). **I**–**III** are designed on a basis of the judicious balance between π -elongation and the stabilization of aromaticity. Upon forming the proton-transfer tautomer in the excited state, using **I** (see Scheme 1) as a prototype, the aromaticity of benzene is destabilized by the elongated π -delocalization incorporating four conjugated double bonds (see those double bonds marked in red). According to the theory of effective conjugation length (ECL),⁹ the proton-transfer tautomer with longer π -conjugation (cf. the normal form) is expected to have smaller S_1' – S_0' (prime denotes the proton-transfer tautomer) energy gap (cf. normal S_1 – S_0). The interplay between π -conjugation and aromaticity is more significant in **II** and **III** because of the partial reduction of aromaticity in the fused benzene and naphthalene, respectively, in order to fulfill extended five effective π -conjugated bonds (see Scheme 1). The proton-transfer tautomer of **II** (relative to normal form) is

Scheme 2. Synthetic Routes of III^a

^a See experimental section for the detail of synthesis.

predicted to be more unstable than that of **III**, due to more energy needed to reduce the aromaticity of benzene (in **II**) than that of the naphthalene moiety (in **III**).¹⁰ Accordingly, the relative energy between normal and tautomer in the excited state can be systematically fine-tuned among **I**, **II**, and **III**. As a result, for **II** and **III** excited-state equilibrium is established between normal and tautomer forms. White light generation is achieved serendipitously in a single ESIPT system **III**. Detail of synthesis, photophysical properties, and OLED application is elaborated as follows.

2. EXPERIMENTAL SECTION

2.1. Synthesis and Characterization. Except for acetonitrile-*d*₃ (Cambridge Isotope Laboratories, Inc.), other solvents were purchased from Merck and distilled from appropriate drying agents prior to use. Commercially available reagents were used without further purification unless otherwise stated. All reactions were monitored by thin-layer chromatography (TLC) with Macherey–Nagel precoated Glassic sheets (0.20 mm with fluorescent indicator UV254). Compounds were visualized with UV light at 254 and 365 nm. Flash column chromatography was carried out using silica gel from Merck (230–400 mesh).

Compounds **I** and **II** were prepared according to a standard literature procedure,¹¹ for which the characterization is provided in the Supporting Information. 1-Hydroxy-11H-benzo[b]fluoren-11-one (**III**) was synthesized according to a four-step synthetic route depicted in Scheme 2, in which each step is described below.

2.1.1. 3-Bromo-7-methoxy-2,3-dihydro-1H-inden-1-one (4). 7-Methoxy-2,3-dihydro-1H-inden-1-one (1.0 g, 6.2 mmol) and *N*-bromosuccinimide (1.2 g, 6.8 mmol) were dissolved in 20 mL of CCl₄, and 12 mg (1 mol %) of 2,2'-azobisisobutyronitrile (AIBN) was added. The mixture was slowly stirred and heated to 80 °C for 2 h. After cooling, the mixture was poured into cold water, extracted with CH₂Cl₂, and dried with anhydrous MgSO₄. After the solvent was removed, the crude product was purified by silica gel column chromatography with eluent ethyl acetate/*n*-hexane (1/4) to afford **4** (1.1 g, 74%). ¹H NMR (CDCl₃, ppm) 7.62 (t, *J* = 8.5 Hz, 1H), 7.20 (d, *J* = 8.0 Hz, 1H), 6.87 (d, *J* = 8.5 Hz, 1H), 5.52 (dd, *J*₁ = 7.0 Hz, *J*₂ = 2.0 Hz, 1H), 3.92 (s, 3H), 3.32 (dd, *J*₁ = 18.5 Hz, *J*₂ = 7.0 Hz, 1H), 2.97 (dd, *J*₁ = 18.5 Hz, *J*₂ = 2.0 Hz, 1H). MS (FAB) *m/z* 240 (*M* + *H*)⁺. HRMS calcd for C₁₀H₁₀BrO₂, 240.9864; found, 240.9866.

2.1.2. 7-Methoxy-1H-inden-1-one (3). 3-Bromo-7-methoxy-2,3-dihydro-1H-inden-1-one (1.0 g, 4.1 mmol) in CCl₄ was cooled in an ice bath, and 1.93 mL (1.4 g, 14.0 mmol) of triethylamine was added a slowly. The reaction mixture was allowed to warm to room temperature and stir overnight. After the solvent was removed, the crude product was purified by silica gel column chromatography with eluent ethyl acetate/*n*-hexane (1/4) to afford **3** (0.63 g, 95%). ¹H NMR (CDCl₃, ppm) 7.42 (d, *J* = 6.0 Hz,

1H), 7.34 (t, $J = 8.0$ Hz, 1H), 6.85 (d, $J = 8.8$ Hz, 1H), 6.70 (d, $J = 8.0$ Hz, 1H), 5.84 (d, $J = 6.0$ Hz, 1H), 3.95 (s, 3H). ^{13}C NMR (100 MHz, CDCl_3 , ppm) 196.57, 156.50, 147.38, 147.03, 144.48, 136.02, 127.70, 115.65, 114.67, 55.89. MS (FAB) m/z 161 ($\text{M} + \text{H}$) $^+$. HRMS calcd for $\text{C}_{10}\text{H}_9\text{O}_2$, 161.0603; found, 161.0608.

2.1.3. 1-Methoxy-11H-benzo[*b*]fluoren-11-one (2). A mixture of solution of α,α,α' -terarbro-*o*-xylene (1.3 g, 3.1 mmol), 7-methoxy-1H-inden-1-one (0.5 g, 3.1 mmol), sodium iodide (1.8 g, 12 mmol), and dry DMF (30 mL) was stirred at 65 °C for 24 h. The reaction mixture was poured into cold water (70 mL) containing sodium bisulfite (1.0 g). The yellow precipitate was purified by silica gel column chromatography with eluent ethyl acetate/*n*-hexane (1/4) to afford **2** (0.73 g, 90%). ^1H NMR (CDCl_3 , ppm) 8.14 (s, 1H), 7.79–7.88 (m, 3H), 7.43–7.54 (m, 3H), 7.31 (d, $J = 7.6$ Hz, 1H), 6.85 (d, $J = 8.4$ Hz, 1H), 3.99 (s, 3H). ^{13}C NMR (100 MHz, CDCl_3 , ppm) 191.06, 158.54, 146.83, 137.56, 136.96, 136.50, 133.76, 133.10, 130.58, 128.68, 128.59, 126.78, 125.01, 122.74, 119.03, 113.26, 112.37, 55.89. MS (FAB) m/z 261 ($\text{M} + \text{H}$) $^+$. HRMS calcd for $\text{C}_{18}\text{H}_{13}\text{O}_2$, 261.0916; found, 261.0918.

2.1.4. 1-Hydroxy-11H-benzo[*b*]fluoren-11-one (III). 1-Methoxy-11H-benzo[*b*]fluoren-11-one (300 mg, 1.1 mmol) was dissolved in 10 mL of dichloromethane in a 50 mL round-bottom flask, and the flask was placed in an ice bath at 0 °C. A solution of boron tribromide (0.25 mL, 1.0 M solution in dichloromethane) was added carefully to the stirred solution under a nitrogen atmosphere. After 4 h, the reaction was cooled, and the reaction mixture was then hydrolyzed by carefully shaking it with 10 mL of water and extracted twice with 10 mL of dichloromethane. The combined organic phases were then dried over magnesium sulfate, filtered, and evaporated in vacuo; the crude product was purified by silica gel column chromatography with eluent ethyl acetate/*n*-hexane (1/10) to afford **III** (269 mg, 95%). ^1H NMR (CDCl_3 , ppm) 8.64 (s, 1H), 8.07 (s, 1H), 7.84 (d, $J = 7.5$ Hz, 1H), 7.78 (s, 1H), 7.77 (d, $J = 9.0$ Hz, 1H), 7.54 (t, $J = 7.5$ Hz, 1H), 7.38–7.46 (m, 2H), 7.15 (d, $J = 7.0$ Hz, 1H), 6.76 (d, $J = 8.0$ Hz, 1H). ^{13}C NMR (100 MHz, CDCl_3 , ppm) 195.51, 157.66, 144.25, 137.99, 137.81, 136.74, 133.41, 132.68, 130.78, 129.13, 128.85, 127.08, 125.54, 120.16, 120.01, 117.40, 113.00. MS (FAB) m/z 247 ($\text{M} + \text{H}$) $^+$. HRMS calcd for $\text{C}_{17}\text{H}_{11}\text{O}_2$, 247.0759; found, 247.0755.

2.2. Steady-State and Time-Resolved Fluorescence Spectroscopy. Steady-state absorption and emission spectra were recorded on a Hitachi (U-3310) spectrophotometer and an Edinburgh (FS920) fluorimeter, respectively. Both the wavelength-dependent excitation and the emission response of the fluorimeter were calibrated.

Time-resolved spectroscopic measurements were carried out by means previously reported elsewhere in detail.¹² In brief words, sub-ns to ns time-resolved studies were performed using a time-correlated single photon counting (TCSPC) system (OB-900 L lifetime spectrometer, Edinburgh) with the excitation light from either second harmonic generation (SHG, at 400 nm) or third harmonic generation (THG, at 266 nm) of pulse-selected femtosecond laser pulses at 800 nm (Tsunami and Model 3980 pulse picker, Spectra-Physics). The fluorescence was collected at a right angle with respect to the pump beam path and passed through a polarizer, setting the polarization at the magic angle (54.7°) with respect to the pump polarization, and located in front of the detector to eliminate anisotropy. The temporal resolution, after partial removal of the instrument time broadening, is ~ 30 ps. Ultrafast spectroscopic studies were performed by a femtosecond fluorescence up-conversion system (FOG100, CDP) pumped by the same femtosecond oscillator. In the experiment, fluorescence from a rotating sample cell, following the excitation by SHG of a femtosecond pulse, was collected, focused, and frequency summed in a BBO crystal, along with an interrogation gate pulse at designated delay time with respect to the pump pulse. A $\lambda/2$ waveplate was used to set the polarization between pump and gate pulses at magic angle (54.7°) to prevent fluorescence anisotropy contributed by solute reorientation. Fluorescence up-conversion data were fitted to the sum of exponential functions convoluted with the

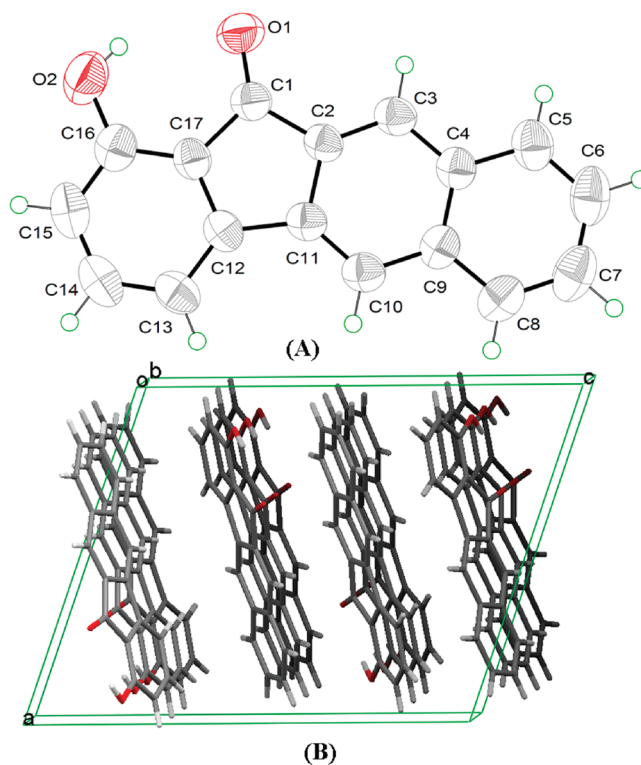


Figure 1. (A) Molecular structure of **III** with thermal ellipsoids drawn at the 50% probability level. (B) Packing view of **III**, viewed along the *b* axis.

instrument response function, which was determined by measuring the Raman scattering signal.

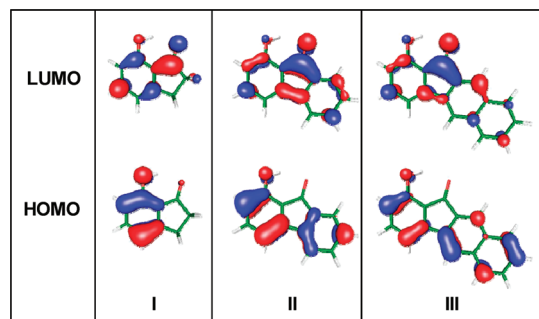
2.3. Computational Methodology. All the theoretical calculations were performed with the Gaussian 03 program.¹³ Geometry optimization for the ground state of molecules **I**–**III** in cyclohexane solution (PCM model)¹⁴ was performed using density functional theory (DFT) with B3LYP¹⁵ hybrid function. For the first singlet excited state, we calculated the Franck–Condon states with time-dependent density functional theory (TD-DFT) using the B3LYP hybrid function. The 6-311+G(d,p) basis sets¹⁶ were employed for all atoms.

2.4. OLED Device Fabrications. All chemicals were purified through vacuum sublimation prior to use. The OLEDs were fabricated through vacuum deposition of the materials at 10^{-6} Torr onto ITO-coated glass substrates, having a sheet resistance of $15 \Omega \cdot \text{sq}^{-1}$. The ITO surface was cleaned ultrasonically—sequentially with acetone, MeOH, and deionized water, followed by the treatment with UV-ozone. A hole-injection layer (PEDOT–PSS) was spin coated onto the substrates and dried at 130 °C for 30 min to remove residual water. Organic layers were then vacuum deposited at a deposition rate of ca. $1\text{--}2 \text{ \AA s}^{-1}$. Subsequently, LiF was deposited at 0.1 \AA s^{-1} and then capped with Al (ca. 5 \AA s^{-1}) through shadow masking without breaking the vacuum. The *J*–*V*–*L* characteristics of the devices were measured simultaneously using a Keithley 6430 source meter and a Keithley 6487 picoammeter equipped with a calibration Si-photodiode in a glovebox. EL spectra were measured using a photodiode array (OTO SD1000) with a spectral range from 300 to 1100 nm and a resolution of 1.5 nm.

3. RESULTS AND DISCUSSION

Compounds **I** and **II** were prepared according to a standard literature procedure.¹¹ Synthetic route of **III** is depicted in Scheme 2. In brief, the synthesis of **III** started from a bromination

Scheme 3. Calculated Frontier Orbitals for I, II, and III of Normal Form Involved in the First Singlet Excitation by B3LYP/6-311 + G(d,p)/PCM



of 7-methoxy-2,3-dihydro-1*H*-inden-1-one (**5**), followed by the elimination of the bromo adduct (**4**), giving a reactive dienophile **3**. The naphthalene moiety was then fused onto the C₂–C₃ double bond (see Scheme 1) by placing **3** through a reaction with tetrabromo-*o*-xylene,¹⁷ yielding **2**. Compound **2** was then subject to the deprotection with BBr₃ to give **III** an overall product yield of 60%. The structure of **III** was further confirmed by single-crystal X-ray diffraction analysis. As shown in Figure 1A, the molecular structure of **III** is nearly planar, which is also confirmed by geometry optimization in our DFT calculation (see Scheme 3). This, together with 2.879 Å of O(2)–O(1) distance, supports the existence of a six-membered ring intramolecular hydrogen bond. However, in the ¹H NMR spectrum (in CDCl₃), as opposed to the large downfield shift ($\delta > 10$ ppm) of the –OH proton in most ESPT molecules possessing strong intramolecular hydrogen bond,¹ the –OH proton signal of **III** appears at δ 8.64 ppm, revealing a relatively weaker hydrogen-bond formation. This is possible due to the fact that the carbonyl oxygen (O(1), see Figure 1) sits at the five-membered ring cyclopenta-2,4-dienone moiety, such that the \angle O(2)–H–O(1) angle is expected to be deviated from 120°, a perfect six-member ring hydrogen-bonding formation. This viewpoint is supported by the \angle O(2)–H–O(1) angle of 142.6°, according to the X-ray structure analysis. Careful examination of the crystal structure also indicates that there exists substantial π – π stacking between the tetracyclic plane and its adjacent one, so the molecules are packed into layers along the *b* axis shown in Figure 1B.

Steady-state absorption and emission spectra of compounds I–III in cyclohexane at room temperature are depicted in Figure 2. Pertinent data are listed in Table 1. **I** exhibits the lowest lying absorption band maximized at 315 nm, attributed to a π – π^* transition, which is also supported by the calculated frontier orbitals shown in Scheme 3. Scheme 3 also reveals that the electron density around the intramolecular hydrogen binding site is mainly populated at hydroxyl oxygen and carbonyl oxygen at highest occupied molecular orbital (HOMO) and lowest unoccupied molecular orbital (LUMO), respectively. The results clearly indicate that upon electronic excitation of all I–III, the hydroxyl proton is expected to be more acidic, whereas the carbonyl oxygen is more basic with respect to their ground state, driving the proton-transfer reaction.

Experimentally, upon excitation, a large Stokes-shifted emission maximized at \sim 530 nm is resolved for **I** in cyclohexane. The similar excitation and absorption spectral profiles (see Figure S1a, Supporting Information) conclude the same ground-state origin

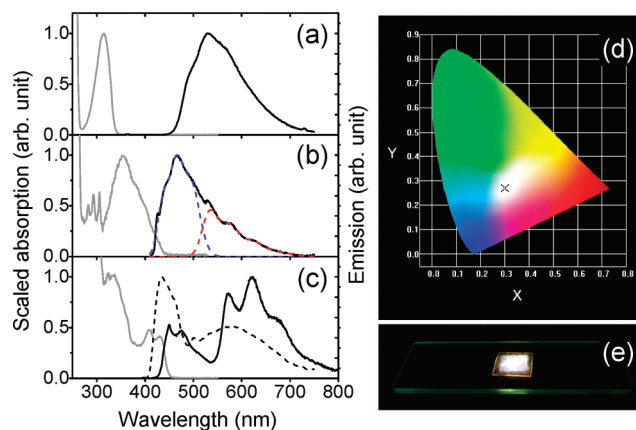


Figure 2. Solid lines: steady-state UV–vis absorption spectra (gray) and photoluminescence spectra (black) of (a) **I**, (b) **II** and (c) **III** in cyclohexane. Dotted lines in (b) depict the decomposed PL spectra assigned for normal (blue) and tautomer (red) species, respectively. Dashed line in (c) depicts the PL spectrum of amorphous solid powder sample **III**, whose corresponding calculated CIE 1931 chromaticity coordinates ($x = 0.30$, $y = 0.27$) is shown in (d). The photograph in (e) shows, in the dark room, a piece of solid vinyl matrix doped with **III** and shed with laboratory UV lamp (366 nm) through a square mask underneath.

for the emission. The difference in peak wavelength between absorption and emission of as large as $\sim 13,000$ cm^{–1} unambiguously supports the occurrence of ESPT, forming a proton-transfer tautomer adiabatically in the excited state. Further attempts to resolve the dynamics of ESPT were made by using a time-correlated single-photon counting system with 266 nm excitation. The result (see Figure S1b, Supporting Information) reveals that the tautomer emission of **I** (monitored at 550 nm) consists of a rise component that is beyond the limit of our system response (< 30 ps), followed by a population decay time resolved to be 1.0 ns. Upon monitoring at, e.g., 370 nm, which is supposed to be in the normal emission region and is barely shown in the steady-state measurement, a fast, irresolvable decay component of < 30 ps was also acquired. Unfortunately, the lowest lying absorption of < 350 nm for **I** makes further femtosecond time-resolved study, such as fluorescence up-conversion, infeasible, mainly due to the lack of excitation wavelength in the current set up. Nevertheless, both steady-state and picosecond time-resolved measurements lead us to conclude an ultrafast, exergonic type of ESPT for **I**, similar to most of the reported ESPT molecules.¹

In stark contrast, as shown in Figure 2b, dual emission seems to be resolved in the steady-state measurement of **II**, which upon deconvolution, is composed of a normal emission, justified by its mirror image with respect to the lowest lying absorption, and a large Stokes shifted tautomer emission band maximized at 468 and 535 nm, respectively (also see deconvoluted curve in Figure 2b). In **III**, both normal ($\lambda_{\text{max}} \sim 450$ nm) and tautomer ($\lambda_{\text{max}} \sim 620$ nm) emissions are well distinguished. The early time relaxation dynamics of the normal emission for both **II** and **III** were measured by femtosecond fluorescence up-conversion ($\lambda_{\text{ex}}: \sim 400$ nm). The resulting relaxation dynamics, shown in Figure 3 and Table 1, consist of a fast decay with a time constant of 8.2 ps for **II** and 15 ps for **III**, followed by a much longer population decay component. Upon monitoring tautomer emission, the relaxation pattern consists of a rise component, 1.9 and 8.3 ps for **II** and **III**, respectively, followed by a long population decay

Table 1. Photophysical Properties of I–III in Cyclohexane at Room Temperature

	steady-state measurement		time-resolved measurement		
	λ_{abs} [nm]	λ_{em} [nm] (Q.Y.)	λ_{monitor}	fitted time constants (prefactor) by femtosecond fluorescence up-conversion	population decay time by TCSPC
I	315	530 (0.012)	550 nm		1.0 ns
II	354	468 (0.019)	440 nm		1.2 ns
		535 (0.014)	480 nm	8.2 ps (0.27), 1.2 ns (0.73) ^a	
			620 nm	1.9 ps (−0.34), 32 ps (0.16), 1.2 ns (0.50) ^a	1.2 ns
III	409	450 (0.006)	480 nm	15 ps (0.69), 0.66 ns (0.31) ^a	0.67 ns
			620 nm	8.3 ps (−0.44), 0.66 ns (0.56) ^a	
		621 (0.020)	650 nm		0.66 ns

^a Population decay time constant was applied for the fitting.

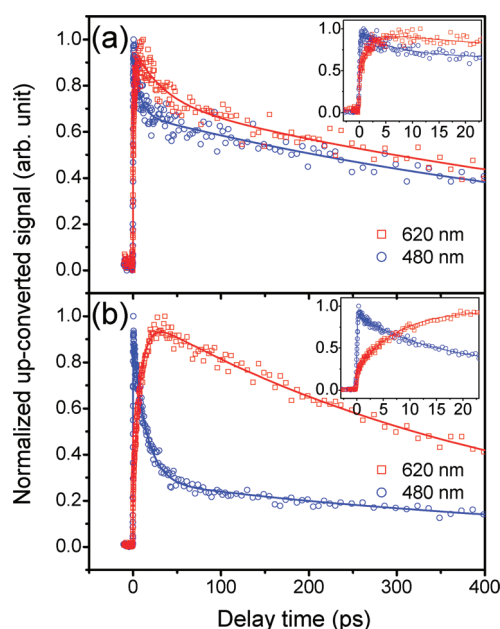


Figure 3. Fluorescence up-conversion decay curves obtained in cyclohexane of (a) II and (b) III. The excitation is at 400 nm and the data points (○ and □) shown are with monitored emission wavelength as depicted. Solid lines depict the best polyexponential fits. The fitting results are summarized in Table 1.

component. The results of subnanosecond time-correlated single-photon counting experiments are shown in Figure 4, which resolve the population decay of the normal emission to be 1.2 and 0.67 ns for II and III, respectively. These time scales, within experimental error, are identical with that of the corresponding tautomer emission, i.e., 1.2 ns in II and 0.66 ns in III. The results are thus fitted to a reaction pattern, depicted in Scheme 4, involving ESIPT upon excitation, followed by an establishment of fast equilibrium prior to the population decay for both normal and tautomer excited states.

According to the reaction model shown in the Scheme 4, the differential rate equations for change of concentrations of normal and tautomer species can be expressed as follows:¹⁸

$$\frac{d[N^*]}{dt} = -(k_{N^*} + k_{\text{pt}}) \cdot [N^*] + k_{-\text{pt}} \cdot [T^*] \quad (1)$$

$$\frac{d[T^*]}{dt} = -(k_{T^*} + k_{-\text{pt}}) \cdot [T^*] + k_{\text{pt}} \cdot [N^*] \quad (2)$$

The coupling eqs 1 and 2 can be solved with given initial conditions, $[N^*](t) = [N^*]_0$ and $[T^*](t) = [T^*]_0 = 0$ at $t = 0$ and the assumption of k_{pt} and $k_{-\text{pt}} \gg k_{N^*}$ and k_{T^*} :

$$[N^*] = \frac{[N^*]_0}{\lambda_2 - \lambda_1} \cdot [(\lambda_2 - X) \cdot e^{-\lambda_1 t} + (X - \lambda_1) \cdot e^{-\lambda_2 t}] \quad (3)$$

$$[T^*] = \frac{k_{\text{pt}} \cdot [N^*]_0}{\lambda_2 - \lambda_1} \cdot [e^{-\lambda_1 t} - e^{-\lambda_2 t}] \quad (4)$$

where,

$$\lambda_1 = \frac{(X + Y) - \sqrt{(X - Y)^2 + 4 \cdot k_{\text{pt}} \cdot k_{-\text{pt}}}}{2} \quad (5)$$

$$\lambda_2 = \frac{(X + Y) + \sqrt{(X - Y)^2 + 4 \cdot k_{\text{pt}} \cdot k_{-\text{pt}}}}{2} \quad (6)$$

with $X = k_{\text{pt}} + k_{N^*}$ and $Y = k_{-\text{pt}} + k_{T^*}$.

Under the assumption that there exists a fast, excited-state equilibrium between the normal and tautomer species (i.e., k_{pt} and $k_{-\text{pt}} \gg k_{N^*}$ and k_{T^*}), $X \approx k_{\text{pt}}$ and $Y \approx k_{-\text{pt}}$, eq 5 and 6 can be written as follows:

$$\lambda_1 = \frac{k_{N^*} \cdot k_{-\text{pt}} + k_{T^*} \cdot k_{\text{pt}}}{k_{-\text{pt}} + k_{\text{pt}}} = \frac{k_{N^*} + k_{T^*} \cdot K_{\text{eq}}}{1 + K_{\text{eq}}} \quad (7)$$

$$\lambda_2 = k_{\text{pt}} + k_{-\text{pt}} \quad (8)$$

The pre-exponential factors in eq 3 for the normal emission can be derived further as

$$[N^*]_0 \cdot \frac{X - \lambda_1}{\lambda_2 - \lambda_1} \approx \frac{k_{\text{pt}}}{k_{\text{pt}} + k_{-\text{pt}}} \quad (9)$$

$$[N^*]_0 \cdot \frac{\lambda_2 - X}{\lambda_2 - \lambda_1} \approx \frac{k_{-\text{pt}}}{k_{\text{pt}} + k_{-\text{pt}}} \quad (10)$$

The equilibrium constant K_{eq} ($k_{\text{pt}}/k_{-\text{pt}}$) for tautomer versus normal species in the excited state is then obtained by dividing eq 9 with eq 10. As a result, the equilibrium constants are calculated to be 0.37 and 2.2, respectively, corresponding to the free energy change of 0.59 and −0.47 kcal/mol between normal and tautomer species for II and III, respectively. Furthermore, the k_{pt} and $k_{-\text{pt}}$ can be derived as $(30 \text{ ps})^{-1}$ and $(11 \text{ ps})^{-1}$,

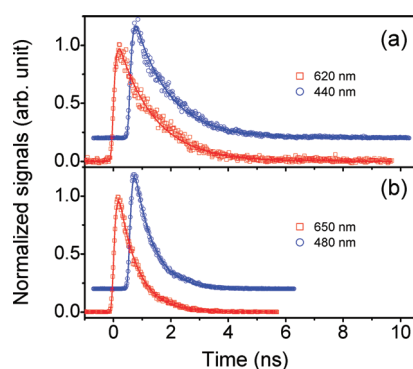
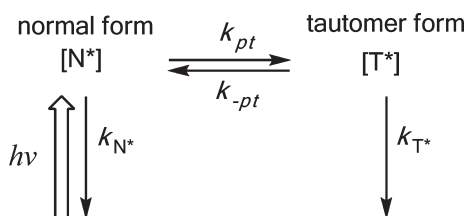


Figure 4. TCSPC measurements of (a) **II** and (b) **III** in cyclohexane with excitation at 400 nm. Open squares (\square) and open circles (\circ , offset for clarity) are data points obtained with monitored emission wavelength as depicted, while solid lines are corresponded convoluted fitting curves of single-exponential function to the data. See Table 1 for fitting results.

Scheme 4. Schematic ESIPT Reaction^a



^a $[N^*]$: concentration of normal species of excited state; $[T^*]$: concentration of tautomer species of excited state; k_{pt} : proton transfer rate constant; k_{-pt} : reverse proton-transfer rate constant; k_{N^*} : decay rate constant of N^* for all decay channel except k_{pt} ; k_{T^*} : decay rate constant of T^* for all decay channel except k_{-pt} .

respectively for **II** and $(21 \text{ ps})^{-1}$ and $(48 \text{ ps})^{-1}$ for **III**. The higher endergonic ESIPT for **II** may partly explain its weaker tautomer emission due to a lesser thermal population of the tautomer species (see Figure 2). Similar rising kinetics following the pattern of eq 4 can be resolved upon monitoring at the tautomer emission (see Figure 3 and Table 1). However, due to the possible overlap with normal emission, both proton transfer kinetics and the deduction of the equilibrium constants are mainly based on those resolved from normal emission using eq 3.

Supplementary support of the above experimental results is provided by the computational approach. The ground-state potential energies calculated at B3LYP/6-311+G(d,p) level are shown in Scheme S1, Supporting Information. For all **I–III**, the normal form was calculated to be the dominant ground-state species due to its lower energy than the tautomer form by 12 to 14 kcal/mol. Note that our focus in this study is mainly on the relative thermodynamics between normal and tautomer excited states, while the reaction potential energy surface (PES), i.e. the kinetics, is not pursued. As for the reaction thermodynamics, the energy level of the tautomer first excited state compared with the normal form is lower by -5.20 kcal/mol for **I**, while it is higher by 9.50 and 3.60 kcal/mol for **II** and **III**, respectively. Table 2 summarizes the energetics calculated for the ground and first singlet excited states of **I–III**. In yet another approach, we may simply add the experimentally resolved tautomer emission gap

Table 2. Calculated Potential Energy (zero point energy) of First Singlet Excited State (S_1) and Ground State (S_0) for **I–III**

	normal form	tautomer form
I		
S ₁ (hartree)	−498.08423	−498.09250
S ₀ (hartree)	−498.23214	−498.21122
ΔE (kcal/mol) ^a	−5.20 (−6.68) ^b	
II		
S ₁ (hartree)	−650.56476	−650.54962
S ₀ (hartree)	−650.66826	−650.64651
ΔE (kcal/mol) ^a	9.50 (3.48) ^b	
III		
S ₁ (hartree)	−804.20147	−804.19574
S ₀ (hartree)	−804.30266	−804.28167
ΔE (kcal/mol) ^a	3.60 (1.67) ^b	

^a Energy change calculated for ESIPT reaction. ^b Values in parentheses are calculated based on spectroscopic measurements and calculated energies of ground state (S_0).

up to the tautomer ground state. As a result, the energy changes (ΔE) of ESIPT are calculated to be -6.68 , 3.48 , and 1.67 kcal/mol for **I–III**, respectively (see Table 1), the trend of which is consistent with that calculated from the aforementioned TD-DFT. More importantly, in a qualitative manner, the results of both methods correlate well with the experimental results. Both experimental and computational results thus support the interplay between effective π -conjugation length and aromaticity. The partial reduction of aromaticity in the fused benzene and naphthalene for **II** and **III**, respectively, at the C_2 – C_3 position has to be taken into account in order to fulfill five effective π -conjugated bonds for the tautomer species (see Scheme 1). Comparing **II** and **III**, the proton-transfer tautomer of **II** (relative to normal form, ΔE in Table 1) is more endergonic than that of **III**, due to more energy required to destroy the aromaticity of benzene (in **II**) than that of naphthalene (in **III**). Evidently, the energetics of ESIPT have been fine-tuned among **I–III**.

The existence of excited-state equilibrium is also observed in solid state. As shown in Figure 2c, **III** clearly reveals both normal and tautomer emissions maximized at 435 and 580 nm, respectively, which are blue shifted in comparison to those acquired in solution (see Figure 2c). The results are consistent with X-ray crystal analysis, concluding substantial π – π stacking in between the tetracyclic planes. The spectral blue shift can be ascribed to a result of the H-aggregate type of interaction. Incidentally, in the solid state, the dual emission achieves a nearly white light generation with CIE (0.30, 0.27) and an overall PL Q.Y. of ~ 0.1 . We then moved one step further by using **III** to fabricate the device for OLEDs in the configuration ITO/PEDOT–PSS (30 nm)/NPB (15 nm)/TCTA (5 nm)/5 wt % **III** doped CBP (25 nm)/TPBI (50 nm)/LiF (0.5 nm)/Al (100 nm). In this device, PEDOT–PSS functioned as the hole injection layer; 4,4'-bis[N-(1-naphthyl)-N-phenylamino]biphenyl (NPB) was the hole transport layer. To decrease the hole-injection barrier between NPB and the emitting layer, we incorporated a layer of 4,4',4''-tris(N-carbazolyl)triphenylamine (TCTA) because of its appropriately matching HOMO energy level. 4,4'-bis(9-carbazolyl)biphenyl (CBP) is used as host for the **III** emitter.

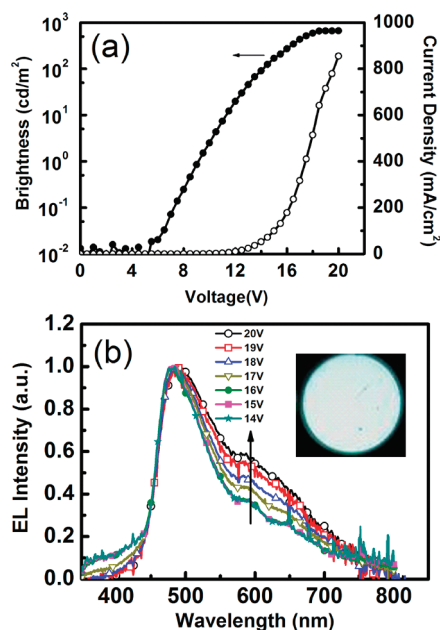


Figure 5. (a) Current density–voltage–luminance (J – V – L) characteristics. (b) EL spectra for devices incorporating **III** as dopant at different voltage. Inset: photo of the device in operation.

1,3,5-Tris(*N*-phenylbenzimidazol-2-yl)benzene (TPBI) functioned as both hole-blocking material and ETL. Lithium fluoride (LiF) was used as the electron-injection layer, and aluminum (Al) was the cathode. In our preliminary test, the device reveals a maximum brightness of 665 cd m^{-2} at 20 V (885 mA cm^{-2}) as Figure 5a shows. The maximum external quantum efficiency, current, and power efficiency were 0.11%, 0.20 cd A^{-1} , and 0.06 lm W^{-1} , respectively. In Figure 5b, the EL spectrum of **III** presents both normal and tautomer emissions at 488 and 590 nm, respectively, which is close to that acquired in solution (e.g., cyclohexane, see Figure 2c). The result can be rationalized by only 5 wt % of **III** used as dopant in OLEDs, so that **III** is prone to exhibit the π -stacking free behavior.

Figure 5b also displays the EL spectra of **III** recorded at various voltages. The spectra are constant when applied voltage under 16 V. However, the relative intensity of the orange emission increases slightly when the voltage is over 16 V, leading to a slight shift in the CIE coordinates from (0.26, 0.35) to (0.28, 0.40) at 16 and 20 V, respectively. This color shift possibly originates from the energy transfer from the blue (normal excited state) to the orange (tautomer excited state) fluorophore at higher voltage. For this case, one would expect slow reverse proton transfer from tautomer to the normal form in the ground state. This issue is pending further resolution.

At the current stage, due to its relatively low overall PL quantum yield of 0.03 in the doped film of **III**, the EL (or OLED) performance is only decent compared with the work mentioned early utilizing multi-ESIPT moieties. For example, Park and co-workers^{7b,c} have reported the white light OLED comprising a molecular framework that covalently links two ESIPT chromophores. Nevertheless, spectral variation due to different photostability of two ESIPT moieties may still need to be concerned. On the other hand, our results clearly provide the proof of concept that a white light generation is accessible based on a single ESIPT system, which opens a new route of white OLED.

4. CONCLUSION

In conclusion, we report a rational tuning of the energetics for normal versus tautomer species of a series of new ESIPT molecules **I**, **II**, and **III**, based on a judicious balance between destruction of aromaticity and compensation of π -conjugation. As a result, the existence of excited-state equilibrium leads to normal and tautomer dual emission spanning the entire visible region for **III**. Its transformation to the bulk properties is also facile, facilitating the device fabrication. OLEDs based on **III** have been successfully fabricated, achieving a maximum brightness of 665 cd m^{-2} at 20 V (885 mA cm^{-2}) with the CIE coordinates of (0.26, 0.35). Further improvement can be made by introducing a bulky substituent such as the *tert*-butyl group to the tetracyclic moiety of **III** so that the π -stacking can be further minimized. Comparing the recent proposal of utilizing excimer and/or exciplex emission to attain white light emission,¹⁹ the dual emission in the ESIPT system is intrinsic, which is established at the single molecular level in both solution and solid phase. Standing on this basis, not only is fine tuning the energetics of excited-state intramolecular proton transfer of fundamental importance but also paves a new and feasible avenue en route to white light generation.

■ ASSOCIATED CONTENT

S Supporting Information. Additional NMR, time-resolved spectroscopic, crystallographic (CIF), and computational data along with complete ref 13 are provided. This material is available free of charge via the Internet at <http://pubs.acs.org>.

■ AUTHOR INFORMATION

Corresponding Author

kyuchen@fcu.edu.tw; wenhung@mail.ntou.edu.tw; chop@ntu.edu.tw

■ ACKNOWLEDGMENT

We thank National Science Council, Taiwan for the financial support.

■ REFERENCES

- (1) (a) Hsieh, C.-C.; Chou, P.-T.; Shih, C.-W.; Chuang, W.-T.; Chung, M.-W.; Lee, J.; Joo, T. *J. Am. Chem. Soc.* **2011**, *133*, 2932. (b) Hsieh, C.-C.; Jiang, C.-M.; Chou, P.-T. *Acc. Chem. Res.* **2010**, *43*, 1364. (c) Lin, C.-C.; Chen, C.-L.; Chung, M.-W.; Chen, Y.-J.; Chou, P.-T. *J. Phys. Chem. A* **2010**, *114*, 10412. (d) Waluk, J. *Conformational Analysis of Molecules in Excited States*; Wiley-VCH: Weinheim, Germany, 2000. (e) Elsaesser, T.; Bakker, H. J. *Ultrafast Hydrogen Bonding Dynamics and Proton Transfer Processes in the Condensed Phase*; Springer: Heidelberg, Germany, 2002. (f) Tanner, C.; Manca, C.; Leutwyler, S. *Science* **2003**, *302*, 1736. (g) Huynh, M. H. V.; Meyer, T. J. *Chem. Rev.* **2007**, *107*, 5004. (h) Fang, C.; Frontiera, R. R.; Tran, R.; Mathies, R. A. *Nature* **2009**, *462*, 200.
- (2) Chen, K.-Y.; Hsieh, C.-C.; Cheng, Y.-M.; Lai, C.-H.; Chou, P.-T. *Chem. Commun.* **2006**, 4395.
- (3) (a) Kuila, D.; Kvakovszky, G.; Murphy, M. A.; Vicari, R.; Rood, M. H.; Fritch, K. A.; Fritch, J. R. *Chem. Mater.* **1999**, *11*, 109. (b) Catalàn, J.; del Valle, J. C.; Clararmunt, R. M.; Sanz, D.; Dotor, J. J. *Lumin.* **1996**, *68*, 165. (c) Tsentalovich, Yu. P.; Snytnikova, O. A.; Forbes, M. D. E.; Chernyak, E. I. S. V.; Morozov, S. V. *Exp. Eye Res.* **2006**, *83*, 1439.
- (4) (a) Sherin, P. S.; Tsentalovich, Yu. P.; Snytnikova, O. A.; Sagdeev, R. Z. *J. Photochem. Photobiol., B* **2008**, *93*, 127. (b) Sherin, P. S.; Grilj, J.; Tsentalovich, Y. P.; Vauthey, E. J. *Phys. Chem. B* **2009**, *113*, 4953.

- (5) Wolfbeis, O. S.; Knierzinger, A.; Schipfer, R. *J. Photochem.* **1983**, *21*, 67.
- (6) Murata, T.; Morita, Y.; Yakiyama, Y.; Fukui, K.; Yamochi, H.; Saito, G.; Nakasuji, K. *J. Am. Chem. Soc.* **2007**, *129*, 10837.
- (7) (a) Kim, S.; Seo, J.; Jung, H. K.; Kim, J. J.; Park, S. Y. *Adv. Mater.* **2005**, *17*, 2077. (b) Kim, S. H.; Park, S.; Kwon, J. E.; Park, S. Y. *Adv. Funct. Mater.* **2011**, *21*, 644. (c) Park, S.; Kwon, J. E.; Kim, S. H.; Seo, J.; Chung, K.; Park, S. Y.; Jang, D. J.; Medina, B. M.; Gierschner, J.; Park, S. Y. *J. Am. Chem. Soc.* **2009**, *131*, 14043. (d) Sun, W. H.; Li, S.; Hu, R.; Qian, Y.; Wang, S.; Yang, G. *J. Phys. Chem. A* **2009**, *113*, 5888. (e) Peng, H.-C.; Kang, C.-C.; Liang, M.-R.; Chen, C.-Y.; Demchenko, A.; Chen, C.-T.; Chou, P.-T. *ACS Appl. Mater. Int.* **2011**, *3*, 1713.
- (8) Chou, P.-T.; Martinez, M. L.; Studer, S. L. *J. Phys. Chem.* **1991**, *95*, 10306.
- (9) (a) Gierschner, J.; Cornil, J.; Egelhaaf, H.-J. *Adv. Mater.* **2007**, *19*, 173–191. (b) Meier, H.; Stalmach, U.; Kolshorn, H. *Acta Polym.* **1997**, *48*, 379–384.
- (10) Wade, L. G. *Organic Chemistry*, 7th ed.; Prentice Hall, Upper Saddle River, NJ, 2009.
- (11) (a) Minuti, L.; Taticchi, A.; Marrocchi, A.; Lanari, D.; Broggi, A.; Gacs-Baitz, E. *Tetrahedron: Asymmetry* **2003**, *14*, 481. (b) Kumar, S.; Murry, R. W. *Tetrahedron Lett.* **1980**, *21*, 4781.
- (12) (a) Chou, P.-T.; Chen, Y.-C.; Yu, W.-S.; Chou, Y.-H.; Wei, C.-Y.; Cheng, Y.-M. *J. Phys. Chem. A* **2001**, *105*, 1731. (b) Chou, P. T.; Pu, S.-C.; Cheng, Y.-M.; Yu, W.-S.; Yu, Y.-C.; Hung, F.-T.; Hu, W.-P. *J. Phys. Chem. A* **2005**, *109*, 3777.
- (13) Frisch, M. J. et al. *Gaussian 03*, revision C.02; Gaussian, Inc.: Wallingford, CT, 2004.
- (14) Cances, M. T.; Mennucci, B.; Tomasi, J. *J. Chem. Phys.* **1997**, *107*, 3032.
- (15) (a) Lee, C.; Yang, W.; Parr, R. G. *Phys. Rev. B* **1988**, *37*, 785. (b) Becke, A. D. *J. Chem. Phys.* **1993**, *98*, 5648.
- (16) Hariharan, P. C.; Pople, J. A. *Mol. Phys.* **1974**, *27*, 209.
- (17) (a) Cava, M. P.; Deana, A. A.; Muth, K. *J. Am. Chem. Soc.* **1959**, *81*, 6458–6460. (b) Mcomie, J. F. W.; Perry, D. H. *Synthesis* **1973**, 416–417.
- (18) (a) Shynkar, V. V.; Mély, Y.; Duportail, G.; Piémont, E.; Klymchenko, A. S.; Demchenko, A. P. *J. Phys. Chem. A* **2003**, *107*, 9522. (b) Chou, P.-T.; Yu, W.-S.; Cheng, Y.-M.; Pu, S.-H.; Yu, Y.-C.; Lin, Y.-C.; Huang, C.-H.; Chen, C.-T. *J. Phys. Chem. A* **2004**, *108*, 6487.
- (19) (a) Zhou, G.; Wang, Q.; Ho, C.-L.; Wong, W.-Y.; Ma, D.; Wang, L. *Chem. Commun.* **2009**, 3574. (b) Williams, E. L.; Haavisto, K.; Li, J.; Jabbour, G. E. *Adv. Mater.* **2007**, *19*, 197. (c) Kalinowski, J.; Cocchi, M.; Virgili, D.; Tattori, V.; Williams, J. A. G. *Adv. Mater.* **2007**, *19*, 4000.